PHYSICAL REVIEW D **109,** 124049 (2024)

Template bank to search for exotic gravitational wave signals from astrophysical compact binaries

Abhishek Sharma,[1,*] Soumen Roy,[2,3,†] and Anand S. Sengupta[1,‡]
[1]*Indian Institute of Technology Gandhinagar, Gujarat 382055, India*
[2]*Nikhef, Science Park 105, 1098 XG Amsterdam, Netherlands*
[3]*Institute for Gravitational and Subatomic Physics (GRASP), Utrecht University, Princetonplein 1, 3584 CC Utrecht, Netherlands*

(Received 6 December 2023; accepted 15 May 2024; published 21 June 2024)

Modeled searches of gravitational wave signals from compact binary mergers rely on template waveforms determined by the theory of general relativity (GR). Once a signal is detected, one generally performs the model agnostic test of GR, either looking for consistency between the GR waveform and data or introducing phenomenological deviations to detect the departure from GR. The nontrivial presence of beyond-GR physics can alter the waveform and could be missed by the GR template-based searches. A recent study [H. Narola *et al.*, Beyond general relativity: Designing a template-based search for exotic gravitational wave signals, Phys. Rev. D **107**, 024017 (2023)] targeted the binary black hole merger, assuming the parametrized deviation in lower post-Newtonian terms, and demonstrated a mild effect on the search sensitivity. Surprisingly, for the search space of binary neutron star (BNS) systems where component masses range from 1 to $2.4M_\odot$ and parametrized deviations span 1σ width of the deviation parameters measured from the GW170817 event, the GR template bank is highly ineffectual for detecting the non-GR signals. Here, we present a new hybrid method to construct a non-GR template bank for the BNS search space. The hybrid method uses the geometric approach of three-dimensional lattice placement to cover most of the parameter space volume, followed by the random method to cover the boundary regions of parameter space. We find that the non-GR bank size is ∼15 times larger than the conventional GR bank and is effectual toward detecting non-GR signals in the target search space.

DOI: 10.1103/PhysRevD.109.124049

I. INTRODUCTION

With the advent of terrestrial observatories such as Advanced LIGO [1], Advanced Virgo [2], and KAGRA [3], the gravitational waves (GWs) from compact binary coalescences (CBCs) [4–6] allow us to conduct tests of General Relativity (GR) [7–11]. In addition to GWs, GR has also been tested using Solar System observations [12], binary pulsar observations [13–15], and observations of supermassive black holes at the center of galaxies [16–18]. None of them has found any statistically significant deviation yet, which concludes that GR is the most accurate theory of gravity known to date. In particular, compact binary mergers can probe gravity at its most extreme environment characterized by highly dynamical, nonlinear, and genuinely strong-field regime. Therefore, such systems are exceptional laboratories for unraveling the beyond-GR physics.

The observations and tests of beyond-GR physics with CBCs can be designed by availing the accurately modeled waveforms for beyond-GR theories. Unfortunately, one lacks a complete understanding of the dynamics of coalescing compact binary in the strong-field regime, in nearly all alternative theories of gravity. Recently, there has been progress toward numerical relativity (NR) simulations of binary black hole mergers in theories beyond GR [19–21]. Some of these simulations approximately solve the underlying field equations. In addition to some early developments on the NR front, several efforts have been made to obtain the analytical gravitational waveforms in alternative theories [22–26]. However, a lot more work is still required before these early developments can be incorporated in GW data analysis. Moreover, there might be a more accurate alternative theory, which is unknown to us. Thereby, we generally perform model agnostic analyses: looking for consistency between GR waveform and data [27–31] and introducing phenomenological deviations to detect the departure from GR [32–35]. One example of latter kind of analysis is the *parametrized test* of GR, where one measures the deviations in various post-Newtonian (PN) terms of the GR predicted waveform phase.

All these tests are performed *after* a GW signal is confidently detected by one of the several search pipelines.

---

[*] sharma.abhishek@iitgn.ac.in
[†] soumen.roy@nikhef.nl
[‡] asengupta@iitgn.ac.in

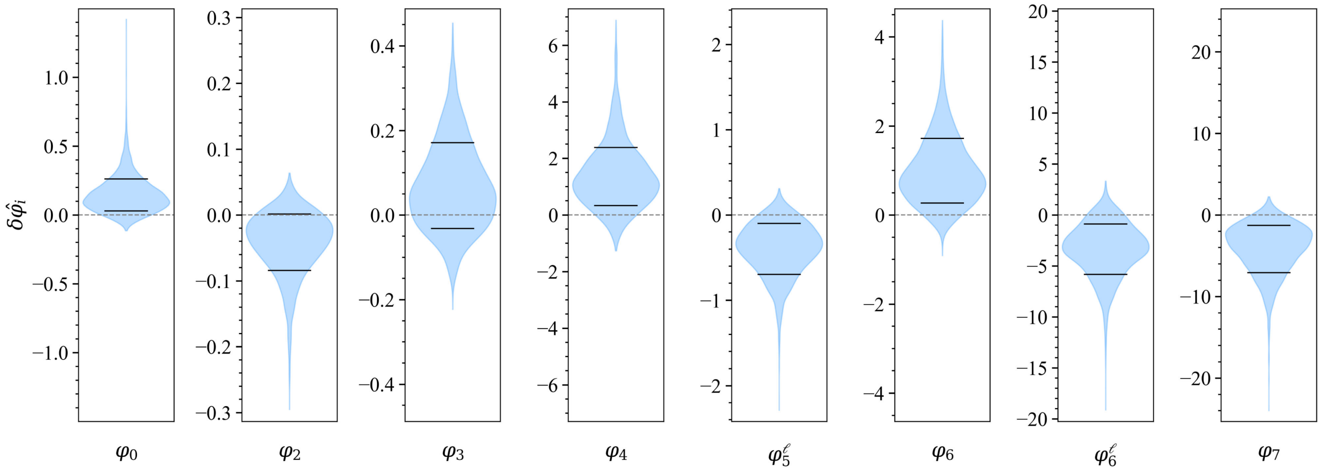

FIG. 1. Posterior distribution for deviation parameters obtained from the parametrized test with GW170817 event [51]. Black horizontal ticks mark the 68% credible interval. The gray horizontal dashed line corresponds to the GR prediction.

The search techniques can be broadly divided into two categories: generic transient searches and template-based searches. The first kind, such as cWB [36,37] and oLIB [38,39], uses minimal assumptions on the GW signature but is inefficient for long-duration signals or when the signal-to-noise ratio (SNR) is low. On the other hand, the template-based searches such as GstLAL [40,41], MBTA [42], PyCBC [43–45], and SPIIR [46] completely rely on the GR template waveform and are highly efficient for long duration signals. However, a gravitational wave signal carrying a significant amount of non-GR physical effects [in terms of nonzero deviation in the GR-predicted PN phasing coefficient(s)], could be missed by the GR template-based search pipelines.

A recent study [47] demonstrated a method for a *bottom-up* search for the GW signals that may carry deviations in the PN phasing coefficients from the template waveforms predicted by GR. The study highlighted that the GR bank would fail to detect such a non-GR signal and further showed an improvement in sensitivity for detecting non-GR signals when searched using a non-GR template bank. The study focused on the stellar mass binary black hole (BBH) systems ($m_{1,2} \in [5, 50] M_\odot$). The parametrized deviations were considered only in the lower PN terms (up to 2PN) over a range spanning the 90% credible interval of the posterior distribution reported in the test of GR using events in the GWTC-1 [9]. The fitting factor[1] study of the GR template bank for non-GR injections revealed that 20% of injections were recovered below the bank's minimal match of 0.97 [49].

In this paper, we target the search space of binary neutron star (BNS) systems with LIGO's sensitivity in the second observing run (O2)[2] and consider fractional deviations in all of the eight PN terms of the waveform phase up to 3.5PN. Since we are unaware of any astrophysical population in the literature that describes the distribution of parametrized deviations, we consider the 1σ (68%) credible interval of posterior distribution reported in the test of GR with GW170817 [8], as shown in Fig. 1. These posteriors were obtained by varying only a single deviation parameter at a time, since the multiparameter test leads to an uninformative posterior (see, for example, Fig. 7 in Ref. [7]). However, many alternative theories of gravity possess deviation in more than one post-Newtonian term. For example, assuming stationary-phase approximation (SPA), the leading-order term in the waveform phase calculated for Brans-Dicke theory appears at −1PN, and the subleading terms are known from 0PN up to 1.5PN [50]. Therefore, we intend to simultaneously vary all the PN deviation terms to define our non-GR search space. The fitting factor study indicates that the GR template bank for BNS search space is highly ineffectual for detecting the non-GR signals, as shown by the black curve in Fig. 2. Non-GR injections are generated by allowing deviations at all PN orders. None of the non-GR injections is found above the desired fitting factor value of 0.97. Suppose a GW signal from a BNS-like system carries a non-GR effect. In that case, it is likely to be missed by the template-based search pipelines and also the unmodeled search pipelines due to their inefficiency for long-duration signals.

---

[1] The fitting factor of a template bank for an arbitrary signal is defined as the maximum value of match over all the templates [48], given in Eq. (8).

[2] Average multidetector noise PSD: the harmonic mean of the power spectral densities measured from the Hanford and Livingston detectors: https://github.com/gwastro/pycbc-config/tree/65138ade78b234a805e49b694db1c17c20948ecc/O2/psd.

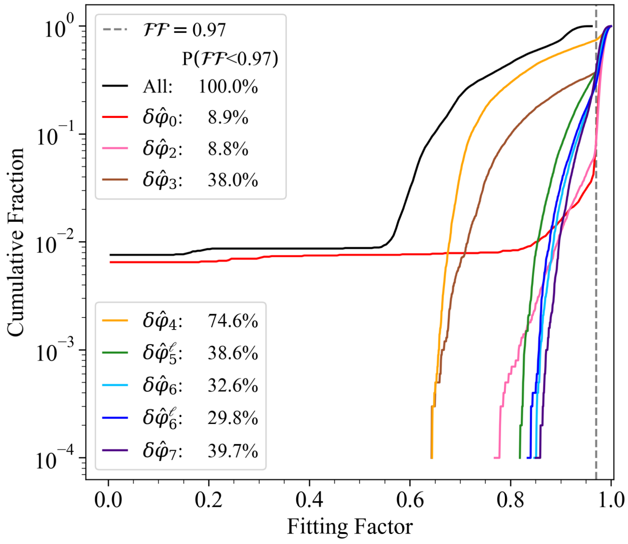

FIG. 2. Cumulative distribution of fitting factor of GR bank for several sets of non-GR signals, each set comprising 10^4 signals. The plot is generated using LIGO's O2 sensitivity curve. The GR template bank for BNS search space is generated assuming the mass-spin parameter ranges given in the first two rows of Table I, and the minimal match is set to be 0.97 [52]. The black curve shows the fitting factor for non-GR signals generated assuming deviations at all PN orders. The rest of the curves shows fitting factor for non-GR signals generated assuming deviation in a particular PN phasing coefficient. The deviation parameters are drawn uniformly within the range given in Table I while generating the non-GR signals. The details of the template bank generation and fitting factor studies are described in Secs. III and IV, respectively.

Figure 2 furthermore shows the fitting factor results for the non-GR signals generated assuming deviation in single parameter. For deviations at lower PN order, namely, at 0PN and 1PN, approximately 9% of injections are recovered with a fitting factor below 0.97. Note that for deviation at 0PN a few injections are recovered with zero fitting factor. For deviation at 1.5PN and higher-order PN terms, more than ∼30% injections are recovered with a fitting factor below 0.97. Interestingly, more than 74% of injections are found below the desired fitting factor for deviation in 2PN.

The fitting factor studies indicate that GW searches using only GR waveforms result in a poor ability to observe BNS systems with non-GR effects. Another approach for detecting GW signals is the unmodeled search, which works without relying on waveform morphology but is inefficient for low-mass binary systems due to their longer in-band duration. As a result, it becomes imperative to develop a beyond-GR search framework, aiming not only to detect new signals but also to explore new aspects of physics.

A crucial input for the matched-filtering search framework is a template bank, which is defined as a collection of theoretical waveforms representing the GWs expected from compact binary mergers. In previous studies, several methods have been proposed to generate a template bank for searches of GW signals from compact binary mergers. The template placement methods are broadly divided into three categories based on their treatment of placement algorithm: geometric, stochastic, and hybrid. The geometric method involves placing templates in the parameter space following a regular, gridlike structure [49,53–58]. This method relies on a parameter space metric that quantifies the mismatch between templates, aiming for uniform coverage. It is efficient for covering a flat parameter space where the metric can be accurately defined. With this method, one can create the most optimal template banks by employing the $\mathcal{A}_n^*$ lattice, which is the best lattice covering in dimensions $n \leq 5$ [53]. This method is extensively used to cover the BNS search space with the TaylorF2 waveform model [55]. However, with the current generation of detectors, the TaylorF2 model is not reliable for detecting the BBH or neutron star-black hole systems due to larger merger-ringdown phase contribution to the signal. The parameter space metric of the full inspiral-merger-ringdown waveform families is not flat. Also, the metric formulation for waveforms with precession or higher harmonics is not known to date. This has led to the development of the stochastic (or so-called random placement) method. The stochastic method generates templates randomly over the parameter space and selects those that maximize coverage while minimizing redundancy [59–61]. As this approach relies on a numerical match function, it is advantageous for exploring complex parameter spaces where the metric is not flat or is unknown. However, its intrinsic random strategy leads to a larger number of templates than needed (so-called overcoverage) and is also computationally intensive. The recent efforts have been focused on developing a hybrid method by combining the space efficiency of the geometric approach with the robustness of the stochastic method [62–67]. The hybrid method is excellent in creating the optimal template banks for the inspiral-merger-ringdown (IMR) waveform families which model the gravitational wave signal from the inspiral, merger, and ringdown stages of the dynamics of a compact binary system and, at the same time, less computationally expensive as compared to the stochastic method. And that has led to its widespread use in the LIGO-Virgo-KAGRA Collaboration [4–6]. This method has been thoroughly developed for nonprecessing binaries; extending them to include eccentricity, higher-order modes, or spin precession effects would greatly enhance searches with future observatories.

The GR search space is characterized by four parameters: the component masses and dimensionless spins of the two components of the binary. In contrast, the non-GR search space is characterized by 12 parameters: the four parameters from the GR model plus eight additional deviation parameters in the PN coefficients (up to 3.5 PN order). A straightforward way to place the templates in

12-dimensional (12D) non-GR parameter space is to use the stochastic approach. However, creating a stochastic template bank for a higher-dimensional parameter space with a larger volume is computationally challenging. In a previous study [47], an eight-dimensional (8D) template bank for non-GR BBH parameter space was indeed constructed using the stochastic approach. It was feasible because the targeted search space volume was small and only four PN deviation parameters (up to the 2PN order) were considered.

In this paper, we introduce a new method to create a non-GR template bank for BNS-like systems where we allow for deviations in all the PN coefficients. Following a study by Brown *et al.* [55], we choose the eight PN phasing coefficients themselves to define the coordinates of an eight-dimensional parameter space, where the parameter space metric becomes flat by construction. Employing principal component analysis, we find that the search space for non-GR signals is effectively three-dimensional (3D) embedded within this aforementioned eight-dimensional parameter space. To construct a template bank, we start by placing a geometric grid over the effective 3D space using the $\mathcal{A}_3^*$ lattice. This geometric grid is further refined by the stochastic placement[3] to ensure adequate coverage across the entire parameter space. Finally, the points in effective 3D space are mapped back to the 12D physical search space using a brute-force method as explained in Sec. III. A companion flow chart outlining our template placement algorithm is illustrated in Fig. 4.

The rest of this paper is organized as follows. In Sec. II, we motivate and describe the search parameter space and the choice of waveform model used to construct the template bank. In Sec. III, we describe in detail the method used to construct the template bank to search for exotic gravitational wave signals. In Sec. IV, we demonstrate the results of validation studies performed to quantify the effectualness of the template banks. Finally, we summarize, conclude, and discuss possible future directions in Sec. V.

II. WAVEFORM MODEL AND SEARCH PARAMETER SPACE

Neutron stars are formed from the collapse of much heavier stars, and in order to conserve angular momentum during collapse, the neutron stars are bound to have large spin at their birth. However, the spinning rate decreases with time due to the magnetic drain of their energy. It is expected to decay away long before entering the band of interest for ground-based gravitational wave observatories [68]. Consequently, previous studies found that aligned spin template waveforms are sufficient for detecting generic spinning BNS systems with second-generation detectors [55]. As the postinspiral and merger signal is emitted at very high frequencies where the second-generation detectors are less sensitive, the signal-to-noise ratio is dominated by the inspiral signal. Therefore, we only consider the inspiral of the two bodies in this work. The inspiral phase of the waveform can be modeled analytically using the PN framework [69]. The waveform in the frequency domain can be expressed as

$$\tilde{h}(f) = \mathcal{A}(f; D_L, \hat{n}, \vec{\lambda}) \exp\{-i\Psi(f; t_c, \phi_c, \vec{\lambda})\}, \quad (1)$$

where D_L is luminosity distance to the source, $\hat{n}$ describes the sky location (α, δ) and polarization angle (ψ) that only affect the overall amplitude and phase of the signal, t_c is the geocentric coalescence time, ϕ_c is the coalescence phase, and $\vec{\lambda}$ refers to the set of intrinsic parameters comprising component masses $(m_{1,2})$ and dimensionless spins $(\chi_{1,2})$. The waveform phase $\Psi(f)$ for TaylorF2 can be expanded as [70,71]

$$\Psi(f) = 2\pi f t_c - \varphi_c - \frac{\pi}{4} + \sum_{k=0}^{7} [\varphi_k(\vec{\lambda}; f_0) + \varphi_k^{\ell}(\vec{\lambda}; f_0) \log x] x^{(k-5)/3}, \quad (2)$$

where $x = f/f_0$ and f_0 is a fiducial frequency. The expansion order k corresponds to $(k/2)$PN term. Various coefficients at different PN orders are given in the Appendix.

All the PN phasing coefficients are uniquely determined for given values of the intrinsic parameters. Any deviation from GR would change the binding energy and angular momentum of the binary and thus transform the equations of binary motion. Alternative theories of gravity will have different functional dependence of PN-phasing coefficients on intrinsic parameters. It has been motivated to devise a parametrized test of GR that works by introducing a fractional deviation parameter $(\delta\hat{\varphi}_i)$ for each phase coefficient φ_i [32,34,72–74],

$$\tilde{\varphi}_i = (1 + \delta\hat{\varphi}_i)\varphi_i^{\mathrm{NS}} + \varphi_i^{\mathrm{S}}, \quad (3)$$

where φ_i^{NS} and φ_i^{S} are the nonspinning and spin-related terms of φ_i, respectively.

A waveform carrying a nonzero deviation parameter is referred to as a *non-GR* waveform. If a gravitational wave signal carries a significant amount of non-GR physical effects, it would be missed by the GR template-based search pipelines as described in Ref. [47], which targeted the BBH search space and allowed deviations in four PN terms from 0.5PN to 2PN order. In this work, we consider the search space of BNS systems and all the deviation parameters up to 3.5PN order. We choose the posterior samples from the parametrized test of GW170817 event studied by LIGO-Virgo-KAGRA (LVK) [8] and consider 1σ interval of the marginal posterior distribution of the

---

[3] We use the top-down part of the hybrid-geometric random template placement method [62].

TABLE I. Parameter ranges used in generating the template bank. The description of parameters below the horizontal dashed line corresponds to the 68% credible intervals of the deviation in PN coefficients obtained from the parametrized analysis on GW170817 as shown in Fig. 1.

Parameter	Limits
Component masses	$m_{1,2} \in [1, 2.4] M_\odot$
Component spins	$\chi_{1,2} \in [-0.05, +0.05]$
Deviation parameters	
0.0 PN	$\delta\hat{\varphi}_0 \in [+0.029, +0.261]$
1.0 PN	$\delta\hat{\varphi}_2 \in [-0.084, +0.001]$
1.5 PN	$\delta\hat{\varphi}_3 \in [-0.032, +0.171]$
2.0 PN	$\delta\hat{\varphi}_4 \in [+0.329, +2.387]$
2.5 PN (log term)	$\delta\hat{\varphi}_5^\ell \in [-0.697, -0.099]$
3.0 PN	$\delta\hat{\varphi}_6 \in [+0.266, +1.715]$
3.0 PN (log term)	$\delta\hat{\varphi}_6^\ell \in [-5.815, -0.881]$
3.5 PN	$\delta\hat{\varphi}_7 \in [-7.067, -1.269]$

deviation parameters to define the boundaries of the non-GR space. Parameter ranges for the template bank construction are tabulated in Table I.

III. TEMPLATE BANK CONSTRUCTION

The long-established method for searching gravitational waves from compact binary mergers relies on the matched filter technique as it is an optimum method to detect a signal if the data contains stationary Gaussian noise. It is accomplished by performing convolution between the data and a set of theoretical filter waveforms to obtain a maximized SNR. In principle, one can maximize the SNR over time, overall amplitude, and overall phase by employing analytical tricks [75–77]. The noise-free response of a LIGO-like detector is given by

$$h(t) = F_+(\alpha, \delta, \psi) h_+(t) + F_\times(\alpha, \delta, \psi) h_\times(t), \tag{4}$$

where h_+ and $h_\times$ are two polarizations of gravitational wave and F_+ and $F_\times$ are the antenna response functions for the two polarizations. For the dominant $(2, \pm 2)$ mode of gravitational wave signals emitted from nonprecessing binary systems, two polarizations are proportional to each other, $\tilde{h}_+ \propto i\tilde{h}_\times$, where $\tilde{h}_{+,\times}$ denotes the Fourier transform of $h_{+,\times}$. Note that this relation deviates when we include the contribution of higher harmonics or precession to the waveform. When this relation holds, the extrinsic parameters such as the sky location, inclination angle, polarization angle, coalescence phase, and distance to the source can all be expressed as overall amplitude and phase. The intrinsic parameters that cannot be absorbed in the analytical maximization procedure, such as component masses and component spins, must be varied to obtain the maximized SNR by generating the filter waveforms repetitively. Our chosen waveform model, TaylorF2, upholds this relation for both the GR and non-GR waveforms. Therefore, we generate the filter waveforms by varying the intrinsic parameters to obtain the optimal SNR. We evaluate the filter waveforms in the parameter space comprising of component masses and component spins for the GR case and over additional eight deviation parameters for the non-GR case. This discrete set of points in the parameter space constitutes a template bank.

When searching for a signal in data d using a template waveform h, the matched filtered SNR is computed by maximizing the inner product between d and h over an overall amplitude, phase (φ_{ref}), and time (t_{ref}),

$$\rho_{\mathrm{MF}} = \max_{t_{\mathrm{ref}}, \varphi_{\mathrm{ref}}} \langle d | \hat{h} \rangle, \tag{5}$$

where $\hat{h}$ is the normalized template waveform such that $\hat{h} = h / \sqrt{\langle h | h \rangle}$ and the inner product $\langle \cdot | \cdot \rangle$ is defined as

$$\langle a | b \rangle = 4 \Re \int_{f_{\mathrm{low}}}^{f_{\mathrm{high}}} \frac{\tilde{a}^*(f) \tilde{b}(f)}{S_n(f)} df, \tag{6}$$

where $S_n(f)$ is the one-sided noise power spectral density. Suppose the template waveform does not *exactly* match the signal in the data even after maximizing over the extrinsic parameters. In that case, we will lose a fraction of SNR, which is determined by the mismatch $(1 - \mathscr{M})$ between them. The quantity $\mathscr{M}$ denotes the match between two waveforms:

$$\mathscr{M}(a, b) = \max_{t_{\mathrm{ref}}, \varphi_{\mathrm{ref}}} \langle \hat{a} | \hat{b} \rangle. \tag{7}$$

To quantify the effectualness of a template bank ($\mathcal{T}$) for detecting an arbitrary signal $h_a(t)$, we calculate the *fitting factor* ($\mathfrak{FF}$), which is defined as maximal match between arbitrary signal and templates in the bank [48],

$$\mathfrak{FF}(h_a) = \max_{\vec{\lambda} \in \mathcal{T}} \mathscr{M}\big(h_a, h(\vec{\lambda})\big), \tag{8}$$

where $\vec{\lambda}$ denotes one of the template points.

A. Parameter space metric

Following Ref. [49], the match between two nearby waveforms, whose intrinsic parameters are infinitesimally separated by $\Delta\vec{\lambda}$, can be Taylor expanded up to the quadratic terms about $\Delta\vec{\lambda} = 0$, which, in turn, can be rearranged to express the *mismatch* $(1 - \mathscr{M})$ in terms of the parameter space metric g_{ij} as

$$1 - \mathscr{M} \simeq g_{ij} \Delta\lambda^i \Delta\lambda^j, \tag{9}$$

where the metric is given by

$$g_{ij} := -\frac{1}{2}\frac{\partial^2 \mathscr{M}}{\partial\Delta\lambda^i \partial\Delta\lambda^j}\bigg|_{\Delta\vec{\lambda}=0}. \tag{10}$$

An alternative approximation for computing the metric is to evaluate the Fisher information matrix of the waveforms over the full parameter space and then project out the dimensions corresponding to the extrinsic parameters [52]. The components of the Fisher information matrix are given by

$$\Gamma_{\alpha\beta} = \left\langle \frac{\partial h(\vec{\theta})}{\partial\theta_\alpha}\middle| \frac{\partial h(\vec{\theta})}{\partial\theta_\beta}\right\rangle, \tag{11}$$

where $\vec{\theta} = \{\vec{\lambda}, \vec{\beta}\}$, such that $\vec{\lambda}$ and $\vec{\beta}$ denote the intrinsic and extrinsic parameters, respectively. The parameter space metric is a crucial input for constructing a geometric template bank in order to compute the distance between two points. When placing the templates, a suitable coordinate system is looked for in which the metric components are almost constant. Under this scheme, a coordinate system with minimum intrinsic curvature is considered good. Following Refs. [55,78], we use the PN phasing coefficients comprising six φ_i and two logarithmic terms φ_i^ℓ given in the Appendix to define the coordinate system. The metric on this 8D parameter space does not have intrinsic curvature—the metric components are constant for any point in parameter space. As described in Refs. [49,55], we similarly use Eq. (10) to first evaluate the metric in nine-dimensional (9D) parameter space including the parameter t_c after maximizing inner product (6) over φ_c; this metric is given by

$$\gamma_{\alpha\beta} = \frac{1}{2}(\mathcal{J}[\psi_\alpha\psi_\beta] - \mathcal{J}[\psi_\alpha]\mathcal{J}[\psi_\beta]), \tag{12}$$

where ψ_α denotes the derivative of the TaylorF2 phase with respect to $\Phi_\alpha \equiv \{t_c, \Phi_i\}$, i.e., $\psi_\alpha = \partial\Psi/\partial\Phi_\alpha$, where the index α ranges from 0 to 8. And Φ_i denotes the eight PN phasing coefficients, i.e., $\Phi_i = \{\varphi_0, \varphi_2, \varphi_3, \varphi_4, \varphi_{5l}, \varphi_6, \varphi_{6l}, \varphi_7\}$. The quantity $\mathcal{J}$ is the moment functional of the noise curve [49,70] and is defined as follows for a given function $a(x)$,

$$\mathcal{J}[a(x)] = \int_{x_L}^{x_H} \frac{a(x)x^{-7/3}}{S_n(xf_0)}dx \bigg/ \int_{x_L}^{x_H}\frac{x^{-7/3}}{S_n(xf_0)}dx, \tag{13}$$

where $x_L = f_{\mathrm{low}}/f_0$ and $x_H = f_{\mathrm{high}}/f_0$ correspond to lowest and highest cutoff frequencies, respectively. The metric g_{ij} on the 8D subspace, composed of PN-phasing coefficients, is obtained by projecting out the coalescence time t_c,

$$g_{ij} = \gamma_{ij} - \frac{\gamma_{0i}\gamma_{0j}}{\gamma_{00}}. \tag{14}$$

The Latin indices i and j range from 1 to 8. This projection operation corresponds to the minimization of the distance $\gamma_{\alpha\beta}\Delta\Phi^\alpha\Delta\Phi^\beta$ with respect to Δt_c [79]. Since the metric g_{ij} in 8D parameter space has no dependence on the parameters (φ_k) itself, therefore, the parameter space is globally flat in terms of these PN-phasing coefficients.

B. Effective dimensionality of the parameter space

The eigenvalues of g_{ij} are rapidly decreasing. In particular, the first two eigenvalues are significantly larger than the remaining ones. That indicates the effective dimension of the parameter space must be lower than the dimension of g_{ij}. The extent of the physically relevant region along many directions in the parameter space must be thinner than the maximum mismatch, and therefore we do not need to place templates in those regions of parameter space.

To identify the effective dimensionality of our parameter space composed of PN-phasing coefficients, we use the principal component analysis-based method proposed in Ref. [55]. We first transform to a Cartesian coordinate system by performing rotation and scaling so that the metric becomes the identity matrix. As a result, further rotations will leave the metric unchanged. As g_{ij} is a real-symmetric matrix, its eigenvectors form an orthonormal basis in $\mathbb{R}^8$. The transformation produces a standard basis given by

$$\tilde{\mu}_i = \sum_j \mathcal{R}_{ij}\mathcal{S}_{jj}\tilde{\varphi}_j, \tag{15}$$

where $\mathcal{R}$ is a rotation matrix such that component $\mathcal{R}_{ij}$ is the jth element of the ith eigenvector and $\mathcal{S}$ is a diagonal scaling matrix, the elements of which are square roots of eigenvalues.

The metric is an identity matrix in this new coordinate system, so we can place the templates using the most optimal $\mathcal{A}_n^*$ lattice. The width of the parameter space is very thin along many directions, and placing templates in 8D parameter space would be suboptimal. Therefore, we perform principal component analysis (PCA) to determine the effective dimension. First, we estimate the covariance matrix in the $\tilde{\mu}_i$ coordinate system by generating a large number of points drawn from uniform distribution within the range of physical parameters as listed in Table I and map them to $\tilde{\mu}_i$ coordinates using Eq. (15). Subsequently, we use eigenvectors of the covariance matrix to transform from $\tilde{\mu}_i$ to principal coordinates given by

$$\xi_i = \sum_j C_{ij}\tilde{\mu}_j, \tag{16}$$

where C_{ij} is the jth element of the ith eigenvector. PCA assures that the maximum parameter space extent would lie along the ξ_1 direction and the least parameter space extent would lie along the ξ_8 direction.

Figure 3 illustrates the extent of parameter space in ξ_i coordinates by depicting a large number of random points

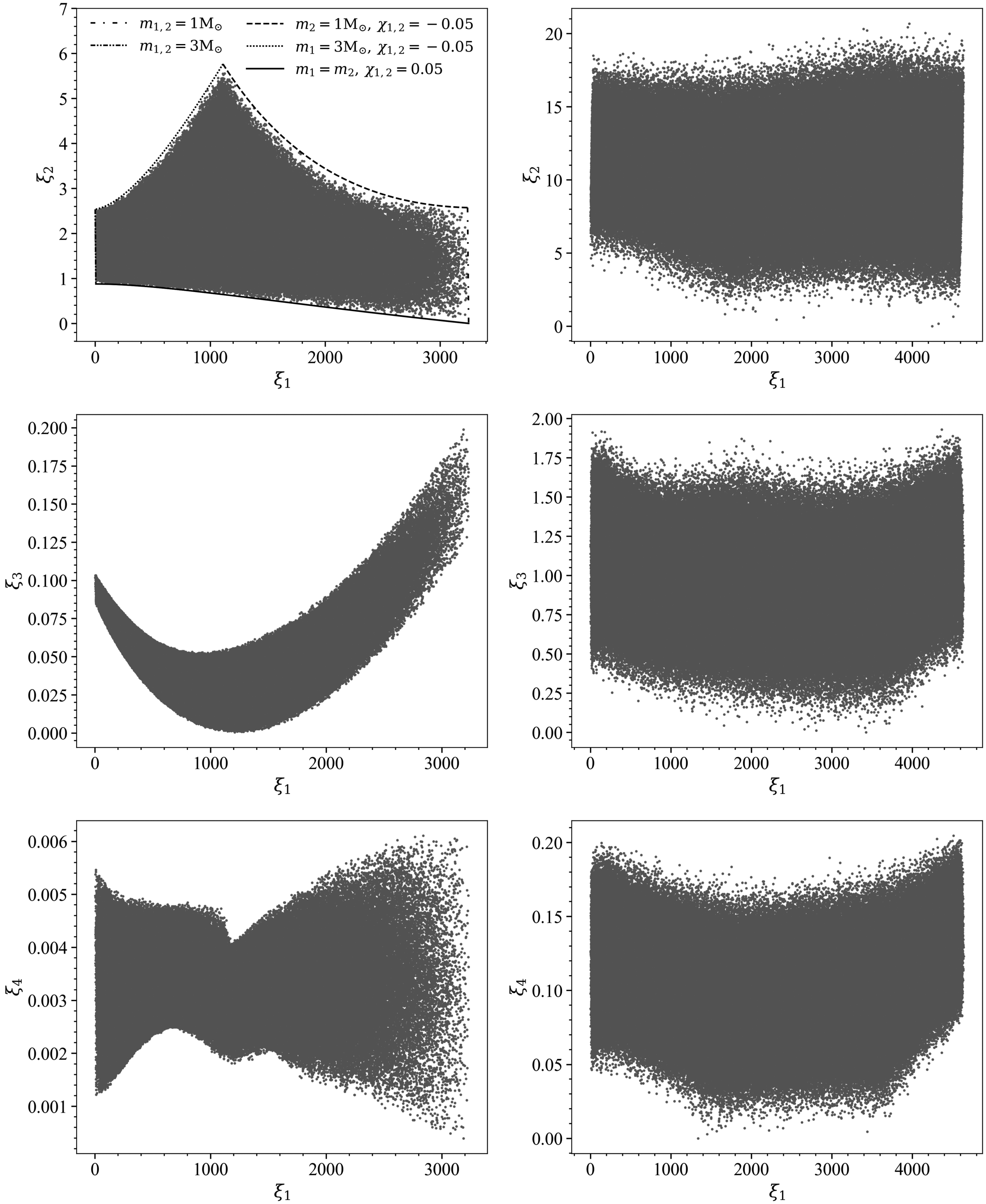

FIG. 3. The width of the parameter space along ξ_2, ξ_3, and ξ_4 directions, plotted against ξ_1 for two distinct cases. Case I (left column): All the deviation parameters ($\delta\hat{\varphi}_i$) are taken to be zero (GR-case). Case II (right column): All deviation parameters are allowed to deviate from zero and their values lie between the ranges given in Table I (non-GR case). Component masses and spins are uniformly distributed between the ranges given in Table I in both cases. Each ξ_i coordinate is scaled such that one unit corresponds to the coverage diameter of 0.97 minimal match contour, $\mathcal{D}_{max}$. The dashed curves in the top left plot marks the boundary of GR parameter space in $\xi_1 - \xi_2$ plane and corresponding physical parameters are given in the legend. The plot is generated using LIGO's O2 PSD with a lower cut-off frequency of 27 Hz.

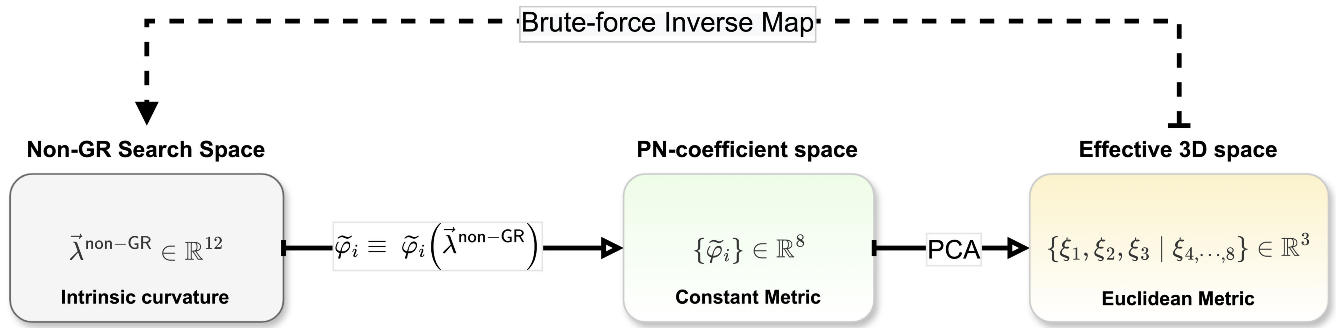

FIG. 4. Schematic representation of various transformations involved in the construction of the non-GR template bank. The non-GR parameter space is described by the component masses $m_{1,2}$, spins $\chi_{1,2}$ and eight deviation parameters ($\delta\hat{\varphi}_i$) and is thus 12D. Using Eqs. (A1) and (3), the 12D vector space is projected to the 8D space of PN-phasing coefficients, which is flat. Finally, in terms of principal coordinates $\{\xi_i\} i = 1, ..., 8$, the dimensionality is found to be effectively three. The parameter space extent along the rest of the five dimensions $\xi_{4,\ldots\times,8}$ is sufficiently small to be ignored. Points in this effective 3D space are mapped back to the physical 12D non-GR parameter space using a brute force method as explained in Sec. III C.

drawn from the uniform distribution of the physical parameters listed in Table I. The figure classifies two cases: the left column shows the extent of GR parameter space where all deviation parameters are set to zero, and the right column refers to the non-GR parameter space that allows deviation parameters to be nonzero. We opt to scale each ξ_i direction such that one unit refers to the coverage diameter of a template, $\mathcal{D}_{\rm max} = 2\sqrt{1 - MM}$, where MM stands for minimal match (0.97). This choice is made to visually identify the effective dimensions for placing the templates. For GR parameter space, one can easily notice that the extent along ξ_3 and ξ_4 directions is smaller than $\mathcal{D}_{max}$, while the directions ξ_1 and ξ_2 carry most of the parameter space extent, so a two-dimensional hexagonal lattice ($\mathcal{A}_2^*$) would be adequate to construct the template bank. On the other hand, for non-GR parameter space, the extent along the ξ_3 is almost twice $\mathcal{D}_{max}$, and the extent along ξ_4 is five times smaller than $\mathcal{D}_{max}$. Therefore, we can place $\mathcal{A}_3^*$ lattice in $\xi_1 - \xi_2 - \xi_3$ coordinates to cover the non-GR search space.

Although we can easily place the templates in ξ_i coordinates using $\mathcal{A}_n^*$ lattice, inverse mapping from ξ_i coordinates to physical parameters has yet to be discovered. On top of this, for the non-GR case, we do not know the parameter space boundaries in ξ_i coordinates, which leads to an additional challenge to construct non-GR template bank. Figure 4 describes a series of coordinate transformations involved in the construction of non-GR template bank.

C. Finding the lattice points in search parameter space

The GR search space is four dimensional, comprising the component masses and spins. The non-GR search space is 12 dimensional due to additional deviation parameters. The template points are generated in ξ coordinates, but there is no inverse mapping to obtain corresponding coordinates in physical search parameter space. Therefore, we follow a brute force method as carried out in previous studies [55,78]. For a given lattice point, this method generates random points in the search parameter space and calculates their distance with the lattice point in ξ space. A random point is considered to be a solution when the distance is less than a predefined tolerance distance (`tol`). Throughout this work, we consider `tol` to be 10^{-2}, corresponding to a mismatch of 10^{-4} as given in Eq. (9). The volume of a sphere with radius `tol` compared to the parameter space volume is $\mathcal{O}(10^6)$ and $\mathcal{O}(10^9)$ times smaller for GR and non-GR cases, respectively. Consequently, finding the solution for all lattice points would be computationally challenging. We alleviate this issue by splitting out the parameter space into nonoverlapping subspaces and using the binary search algorithm KD Tree as implemented in SciPy [80] to find the nearest random point. The conventional partitioning scheme divides the parameter space over the chirp mass. The left panel of Fig. 5 shows two consecutive bins over chirp mass [$\mathcal{M}_c = (m_1 m_2)^{3/5}/(m_1 + m_2)^{1/5}$] for GR parameter space, which are nearly nonoverlapping, while for the non-GR case as shown in the middle panel, the two consecutive chirp mass bins are almost entirely overlapping—it is because of the strong degeneracy between chirp mass and 0PN deviation parameter $\delta\hat{\varphi}_0$. Here, we propose using the 0PN chirp time ($\tilde{\tau}_0$) that depends on $\delta\hat{\varphi}_0$,

$$\tilde{\tau}_0 = \frac{5}{256} \mathcal{M}_c^{-5/3} (\pi f_0)^{-8/3} (1 + \delta\hat{\varphi}_0) \qquad (17)$$

to partition the parameter space in ξ coordinates. The right panel of Fig. 5 shows that $\tilde{\tau}_0$ binning reduces the overlap, but it is less efficient than chirp mass binning for GR space.

We choose those lattice points for which at least one random point is found within `tol` to construct a geometric

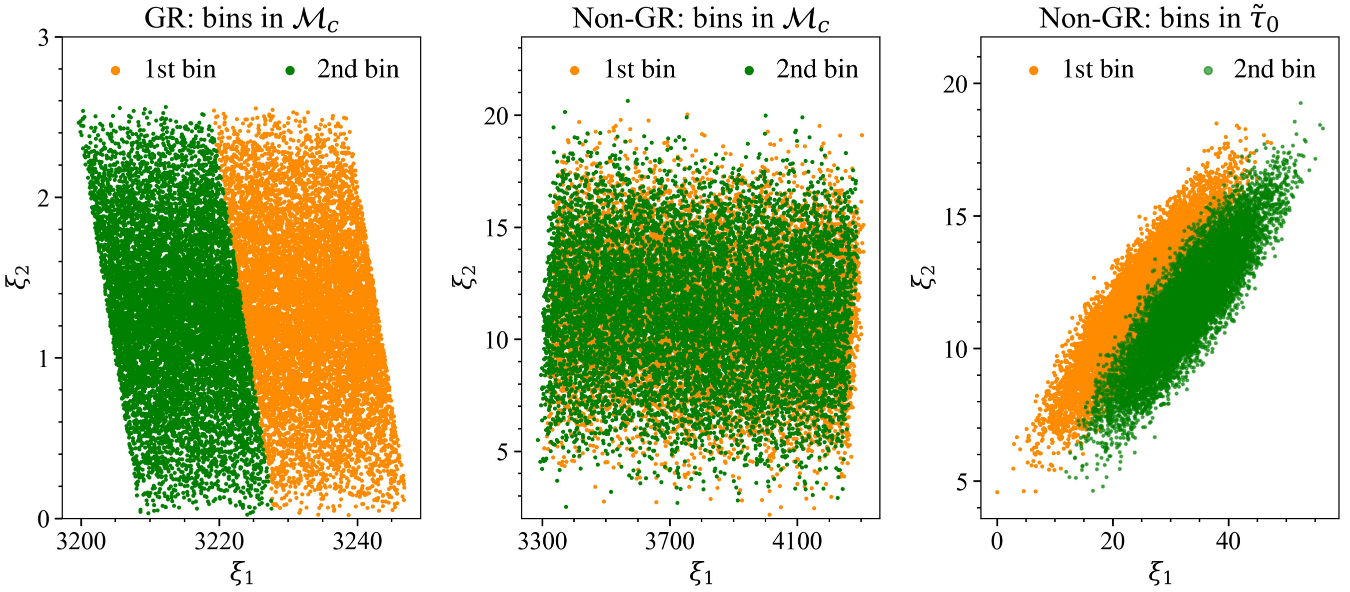

FIG. 5. An illustration of two consecutive bins over two most leading coordinates (ξ_1, ξ_2), which is used to map the lattice points from ξ coordinate to physical parameter space. The left and middle panels show the partitioning in chirp mass $(\mathcal{M}_c)$ for GR and non-GR space, respectively. The chirp mass binning for non-GR parameter space fails to partition the parameter space due to the strong correlation between $\mathcal{M}_c$ and 0PN deviation term $(\delta\hat{\varphi}_0)$. We propose using the 0PN chirp time $(\tilde{\tau}_0)$ as shown in the right panel to partition the non-GR parameter space in ξ coordinates.

template bank. This bank can cover the bulk region of the parameter space, but the boundaries would not be covered adequately. We use the top-down part of the hybrid geometric-random template placement method [62–64] by seeding the precomputed geometric bank. It starts by generating a large number of random points and then removes the points that are located within the distance of $\mathcal{D}_{max}/2$ from the existing templates. Later, it picks one point arbitrarily from the remaining random points as a new template and removes those random points that lie at a distance $\leq \mathcal{D}_{max}/2$ from the chosen point. Continuing this process until all the random points get exhausted generates the hybrid bank. Figure 3 shows the random points that are generated assuming uniform distribution over the parameters listed in Table I, where fewer random points lie near the boundaries. This is more prominent for non-GR case compared to GR. It happens even if we generate points inside a small bin, as shown in Fig. 5. On the other hand, the boundaries of the non-GR parameter space are unknown, and one can cover the boundary region by generating a considerably larger number of random points, but that would be computationally challenging. A suboptimal solution is to generate the random points assuming a uniform distribution in non-GR chirp time coordinates $(\tilde{\tau}_0, \tilde{\tau}_3)$, where $\tilde{\tau}_3$ corresponds to the nonspinning part of the 1.5PN term,

$$\tilde{\tau}_3 = \frac{1}{8\eta f_0}(\pi M f_0)^{-2/3}(1 + \delta\hat{\varphi}_3), \tag{18}$$

where M denotes the total mass of the binary $(M = m_1 + m_2)$.

For construction of the GR bank, we utilize the known boundaries in the $\xi_1 - \xi_2$ plane and generate points using stochastic method along the boundaries. We generate 500 bins over $\mathcal{M}_c$ as described above and simultaneously search for nearest random point for all the lattice as well as the boundary points in each bin on different CPU cores. We find that the (hybrid) GR bank contains 21,766 templates, out of which 15,447 correspond to the $\mathcal{A}_2^*$ star lattice (geometric GR bank) and the rest corresponds to the boundaries. For construction of geometric non-GR bank, we generate 1500 bins over $\tilde{\tau}_0$ as described above and search for nearest solution for lattice points in each bin independently on different CPU cores. This bank contains 284,467 templates. Subsequently, in order to provide coverage near the boundary region, we initialize the top-down part of hybrid random template placement strategy with 200 million random proposals. 84,067 proposals get accepted as new templates resulting in a hybrid non-GR bank with 368,534 templates.

D. Failure of metric approximation—inclusion of exact match

While calculating the overcoverage of the non-GR hybrid bank (see Sec. IV), we inspected the distribution of match between closest pair of templates. More than 22% of templates are found to have the closest point with a match larger than the considered minimal match, as shown in Fig. 8. It indicates a nontrivial overcoverage in the bank.

To comprehend the issue of overcoverage, we spray a large number of points in our parameter space and calculate

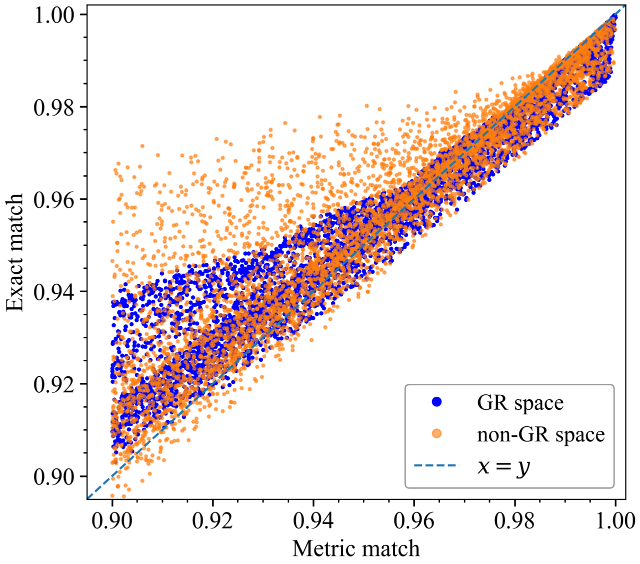

FIG. 6. A comparison between the match calculated using metric approximation as given by Eq. (9) and the exact match as given by Eq. (7), shown for two distinct cases: GR (blue dots) and non-GR (orange dots).

the maximal match of each point with rest of the points using exact match function and the metric (approximate) match as given in Eqs. (7) and (9), respectively. Figure 6 shows the comparison of metric match and the exact match for both GR and non-GR search spaces. For GR search space, we used $\mathcal{A}_2^*$ lattice to place the templates, where the match between the two closest templates (intertemplate match) is expected to be 0.91, but the exact match roughly varies between 0.91 and 0.94. The hybrid method would mostly place the templates near the boundaries, where the intertemplate match can reach up to 0.97, and the corresponding exact match varies between 0.96 and 0.975. Consequently, the GR template bank can have overcoverage, but it is not considerable. Similarly, for the non-GR search space, we used $\mathcal{A}_3^*$ lattice (truncated octahedron) having two kinds of neighbors, one corresponding to square face and other corresponding to hexagonal face (see Appendix B of Ref. [62]). The intertemplate match values for square and hexagonal faced neighbors are 0.904 and 0.928, respectively. Figure 6 suggests that, although a corresponding exact match varies across a wide range of values for the two intertemplate metric match values, only a mild fraction of points can have an exact match above the minimal match (0.97). However, templates added using the hybrid method can have (metric) match values as large as 0.97, where a corresponding exact match can even be larger than 0.98, resulting in the observed overcoverage of hybrid non-GR bank. The large disagreement of the metric and exact match while incorporating the deviation parameters indicates the breakdown of metric approximation.

A recent study [81] described a similar breakdown of Fisher matrix approximation for constructing a template bank for BNS systems with tidal deformability. This study demonstrated that including higher-order terms in the Taylor series expansion of the match function can reliably compute the match. However, it is computationally more expensive than the brute-force computation of the exact match and therefore cannot be used in geometric placement. Following Ref. [63], we use the exact match function as given in Eq. (7) only in the hybrid part of the template placement.

We generate 500 million proposals distributed uniformly in chirp-time coordinates $\{\tilde{\tau}_0, \tilde{\tau}_3\}$, component spins $\{\chi_{1z}, \chi_{2z}\}$, and deviation parameters $\{\delta\hat{\varphi}_i\}$ within their respective limits as given in Table I and use minimal match criteria to be 0.965 while constructing hybrid non-GR bank. 52,885 proposals get accepted as new templates. The inclusion of the exact match and slightly relaxing the minimal match criteria resolves the redundancy issue with 8.5% reduction in bank size. We summarize the size of the geometric and hybrid template banks in Table II.

It takes ∼11, 500 CPU hours to construct geometric non-GR bank. Generation of the hybrid bank, using geometric bank as the seed, takes ∼3500 CPU hours.

TABLE II. Summary of the GR and non-GR template banks that are constructed for BNS systems assuming the parameter ranges tabulated in Table I using TaylorF2 waveform with O2 PSD, and the lower cutoff frequency is set to be 27 Hz. The fourth and fifth columns report the results from bank validity—what percentage of the injections are found with a fitting factor ($\mathfrak{FF}$) below the desired minimal match value of 0.97. The GR bank is highly ineffectual in recovering non-GR signals as none of the injections is recovered above 0.97.

Bank	Type of match computation	Bank size	% of $\mathfrak{FF} < 0.97$		Lowest $\mathfrak{FF}$		Redundancy test % of $\mathfrak{RF} > 0.97$
			GR	Non-GR	GR	Non-GR	
Geometric GR	Metric	15447	1.73	⋯	0.948	⋯	⋯
Hybrid GR	Metric	21766	1.26	100	0.962	⋯	3.9
Geometric non-GR	Metric	284467	⋯	0.52	⋯	0.917	0.0
Hybrid non-GR	Metric	368534	⋯	0.17	⋯	0.95	22.5
Hybrid non-GR	Exact	337352	⋯	0.26	⋯	0.959	0.0

IV. TEMPLATE BANK VALIDITY AND REDUNDANCY

To quantify the performance of the template banks, we carry out Monte Carlo simulations to calculate the distribution of the fitting factor for a large set of injections. The fitting factor value for a waveform tells us what fraction of SNR can be recovered, and the distribution can identify the regions of parameter space where the bank coverage is poor. We generate 10^5 signals using the TaylorF2 waveform model. The intrinsic parameters are drawn from a uniform distribution within their respective boundaries listed in Table I. The fitting factors for nonprecessing binary systems are independent of the extrinsic parameters: the sky location, polarization angle, and inclination angles. Those criteria also holds for non-GR signals. While calculating the fitting factor using Eq. (8), we generate both the template and injection waveforms with a fixed lower cutoff frequency of 27 Hz.

Figure 7 shows the fitting factor distribution of the GR template bank for recovering GR as well as non-GR signals. We note that with the GR bank *all* the non-GR injections are recovered below the fitting factor of 0.97, which implies that the GR template bank is highly ineffectual for detecting the non-GR signals. Figure 7 also shows the fitting factor distributions of the two non-GR banks for recovering non-GR signals. We note that the new hybrid non-GR template bank has recovered *almost all* the injections above a fitting factor of 0.97. We summarize the fitting factor results in Table II.

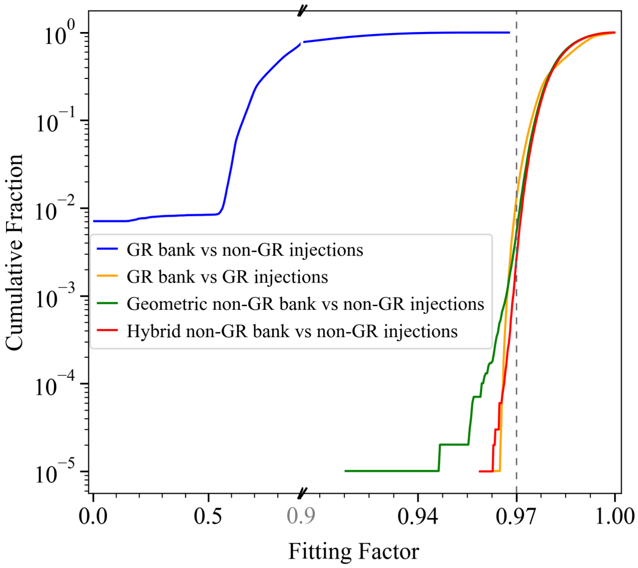

FIG. 7. Effectualness of the template banks for a set of 10^5 TaylorF2 injections generated randomly within their target search spaces described in Table I. We note that for the geometric non-GR bank, although only 0.52% of injections are recovered with a fitting factor below the minimal match of the bank (0.97), it drops to 0.917 for the worst-fitting injection. The complete description of the performance of the banks is listed in Table II. Note that the broken x axis (split at 0.9) is used to accommodate all the fitting factor distributions together.

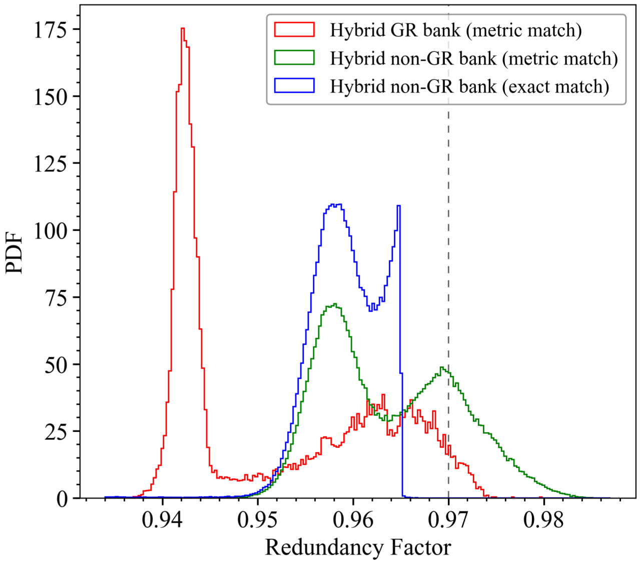

FIG. 8. Redundancy test of GR as well as non-GR banks. Here, the redundancy factor is calculated for every template against the rest of the templates in the bank. The hybrid non-GR bank with the metric match indicates a significant overcoverage, where 22.5% templates are found above the minimal match of the bank (0.97). The complete description of the redundancy test of the banks is listed in Table II.

We perform the redundancy test of a template bank by calculating the maximal match between a targeted template waveform (h_i) and every template waveform (h_j) in the bank excluding the template in question [82]; we call it the redundancy factor ($\mathfrak{RF}$),

$$\mathfrak{RF}(h_i) = \max_{1\le j\le n_{\mathrm{T}},\, j\ne i} \mathscr{M}(h_i, h_j), \tag{19}$$

where n_{T} is the number of templates in the bank. Ideally, the redundancy factor for any template should not be larger than the minimal match used to construct the bank. Figure 8 shows the distribution of the redundancy factor for different template banks. For the hybrid non-GR bank constructed using the metric match, 22.5% of templates have a redundancy factor larger than 0.97, which indicates a significant overcoverage. For comparison, we also construct a similar plot for the GR bank and find that for this case only 3.9% of the templates have the redundancy factor larger than 0.97.

V. DISCUSSION AND CONCLUSION

In this work, we have investigated the performance of a GR-template bank for searching the non-GR signals from BNS systems where component masses range from 1 to $2.4M_\odot$ and the phenomenological deviation parameters span 1σ width of the posterior distribution measured from the GW170817 event. With the LIGO's O2 sensitivity, we have noticed that most of the non-GR signals could be missed by the GR template bank. We have presented a hybrid method for constructing a template bank for searches of beyond GR signals. We found that our non-GR bank size is ∼15 times larger than the conventional GR bank. We have shown that our new bank is faithful in detecting the non-GR signals in its target search space, whereas the GR bank could not recover any non-GR signal above a fitting factor value of 0.97.

The previous study exploring the searches of non-GR signals [47] targeted the search space relevant for BBH systems, and the parametrized deviations were considered in the lower PN terms and constructed an 8D template bank using the straightforward stochastic method. In this work, we target the 12D search space of BNS systems, including the deviation in all the PN terms up to 3.5PN order, and present a hybrid method by combining the space efficiency of the geometric method and the robustness of the random method. In this work, we restrict ourselves to using only the fractional deviations i.e., the deviation over the nonzero PN coefficients. In theory, one can include deviations on the PN terms for which the coefficient value is zero in GR.

This method can be used wherever the TaylorF2 waveform model is applicable, such as searches of subsolar mass compact binary, including eccentricity for subsolar mass/BNS and searches of stellar mass binaries with space-based detectors [82]. While we have constructed the non-GR template bank using the TaylorF2 waveform model in this work, our approach can also be used for IMR waveform models, since our algorithm relies on a "hybrid" method of template placement. Under this approach, one starts by placing an initial geometric grid of templates using the TaylorF2 metric, as generating a geometric bank with the IMR model directly is not feasible. This geometric grid can be further refined by a stochastic placement of additional template points using the "exact match" between new random proposal points and the existing templates in the bank.

The deviation range considered in this work is obtained from LVK analysis of GW170817, which was measured assuming the deviation in a single PN phasing coefficient at a time. Considering deviations in all coefficients simultaneously leads to uninformative posteriors due to correlations among deviation parameters. It might be interesting to consider the uncorrelated non-GR parameters obtained from original deviation parameters through principal component analysis to define the non-GR search space [35,83]. However, the study in Ref. [83] considered the deviations only up to 2PN, and we are unaware of any multiparameter test in the literature that evaluated the deviations in all the PN terms.

In future work, we intend to conduct searches of non-GR signals from BNS-like mergers with the LIGO and Virgo's data during the first and second observation runs. A single detection of this type of source could reveal a novel formation channel for compact binaries.

ACKNOWLEDGMENTS

We thank Ian Harry for carefully reading the manuscript and for offering several comments and suggestions to improve the presentation and content of the paper. We are highly grateful for the suggestions received from Alex Nielsen, Tito Dal Canton, and Thomas Dent. A. S. thanks IIT Gandhinagar for the research fellowship. S. R. was supported by the research program of the Netherlands Organization for Scientific Research (NWO). We acknowledge computational resources provided by IIT Gandhinagar and also thank high performance computing support staff at IIT Gandhinagar for their help and cooperation. We gratefully acknowledge computational resources provided by the LIGO Laboratory and supported by the NSF Grants No. PHY-0757058 and No. PHY-0823459. This research has made use of data, software and/or web tools obtained from the Gravitational Wave Open Science Center, a service of LIGO Laboratory [84], the LIGO Scientific Collaboration, and the Virgo Collaboration. The material of this paper is based upon work supported by NSF's LIGO Laboratory, which is a major facility fully funded by the National Science Foundation. To obtain the waveforms and PN coefficients, we use the LALSIMULATION package of the LIGO Algorithms Library (LAL) software suite [85]. The fitting factor studies were performed by modifying `pycbc_banksim` code implemented in the PYCBC library [86]. Our analysis utilizes NumPy [87], SciPy [80], and Matplotlib [88].

APPENDIX: PN COEFFICIENTS

Here, we describe the PN expansion coefficients of TaylorF2 waveform phase as mentioned in Eq. (2). The waveform phase contains corrections to Newtonian order up to 3.5PN order in nonspinning and linear spin-orbit effects [89,90] and up to 3PN order in quadratic spin effects [91],

$$\varphi_0 = \frac{3}{128\eta}(\pi M f_0)^{-5/3} \tag{A1a}$$

$$\varphi_2 = \frac{3}{128\eta}\left(\frac{3715}{756} + \frac{55\eta}{9}\right)(\pi M f_0)^{-1} \tag{A1b}$$

$$\varphi_3 = \frac{3}{128\eta}\left\{-16\pi + \frac{113\delta\chi_a}{3} + \left(\frac{113}{3} - \frac{76\eta}{3}\right)\chi_s\right\} \times (\pi M f_0)^{-2/3} \tag{A1c}$$

$$\varphi_4 = \frac{3}{128\eta}\left\{\frac{15293365}{508032}+\frac{27145\eta}{504}+\frac{3085\eta^2}{72}+\left(-\frac{405}{8}+200\eta\right)\chi_a^2-\frac{405}{4}\delta\chi_a\chi_s+\left(-\frac{405}{8}+\frac{5\eta}{2}\right)\chi_s^2\right\}(\pi M f_0)^{-1/3} \tag{A1d}$$

$$\varphi_5^\ell = \frac{3}{128\eta}\left\{\frac{38645\pi}{756}-\frac{65\pi\eta}{9}+\delta\left(-\frac{732985}{2268}-\frac{140\eta}{9}\right)\chi_a+\left(-\frac{732985}{2268}+\frac{24260\eta}{81}+\frac{340\eta^2}{9}\right)\chi_s\right\}\log(\pi M f_0) \tag{A1e}$$

$$\begin{aligned}\varphi_6 = \frac{3}{128\eta}\Bigg\{&\frac{11583231236531}{4694215680}-\frac{6848\gamma_E}{21}-\frac{640\pi^2}{3}+\left(-\frac{15737765635}{3048192}+\frac{2255\pi^2}{12}\right)\eta+\frac{76055\eta^2}{1728}-\frac{127825\eta^3}{1296}\\ &-\frac{6848}{63}\log 64+\frac{2270}{3}\pi\delta\chi_a+\left(\frac{2270\pi}{3}-520\pi\eta\right)\chi_s+\left(\frac{75515}{144}\delta-\frac{8225}{18}\delta\eta\right)\chi_s\chi_a\\ &+\left(-480\eta^2-\frac{263245}{252}\eta+\frac{75515}{288}\right)\chi_a^2+\left(\frac{1255}{9}\eta^2-\frac{232415}{504}\eta+\frac{75515}{288}\right)\chi_s^2\Bigg\}(\pi M f_0)^{1/3}\end{aligned} \tag{A1f}$$

$$\varphi_6^\ell = -\frac{107}{42\eta}\log(\pi M f_0)(\pi M f_0)^{1/3} \tag{A1g}$$

$$\begin{aligned}\varphi_7 = \frac{3}{128\eta}\Bigg\{&\frac{77096675\pi}{254016}+\frac{378515\pi\eta}{1512}-\frac{74045\pi\eta^2}{756}+\delta\left(-\frac{25150083775}{3048192}+\frac{26804935\eta}{6048}-\frac{1985\eta^2}{48}\right)\chi_a\\ &+\left(-\frac{25150083775}{3048192}+\frac{10566655595\eta}{762048}-\frac{1042165\eta^2}{3024}+\frac{5345\eta^3}{36}\right)\chi_s\Bigg\}(\pi M f_0)^{2/3},\end{aligned} \tag{A1h}$$

where $\gamma_E \approx 0.577216$ is the Euler constant, $M \equiv m_1 + m_2$ is the total mass of the binary, $\eta \equiv m_1 m_2/M^2$ is the symmetric mass ratio, $\delta \equiv (m_1 - m_2)/M$ is the asymmetric mass ratio, and $\chi_s \equiv (\chi_1 + \chi_2)/2$ and $\chi_a \equiv (\chi_1 - \chi_2)/2$ are the symmetric and asymmetric combinations of the spins.

[1] J. Aasi *et al.* (LIGO Scientific Collaboration), Advanced LIGO, Classical Quantum Gravity **32**, 074001 (2015).

[2] F. Acernese *et al.* (Virgo Collaboration), Advanced Virgo: A second-generation interferometric gravitational wave detector, Classical Quantum Gravity **32**, 024001 (2015).

[3] Y. Aso, Y. Michimura, K. Somiya, M. Ando, O. Miyakawa, T. Sekiguchi, D. Tatsumi, and H. Yamamoto (KAGRA Collaboration), Interferometer design of the KAGRA gravitational wave detector, Phys. Rev. D **88**, 043007 (2013).

[4] B. P. Abbott *et al.* (LIGO Scientific and Virgo Collaborations), GWTC-1: A gravitational-wave transient catalog of compact binary mergers observed by LIGO and Virgo during the first and second observing runs, Phys. Rev. X **9**, 031040 (2019).

[5] R. Abbott *et al.* (LIGO Scientific and Virgo Collaborations), GWTC-2: Compact binary coalescences observed by LIGO and Virgo during the first half of the third observing run, Phys. Rev. X **11**, 021053 (2021).

[6] R. Abbott *et al.* (LIGO Scientific, Virgo, and KAGRA Collaborations), GWTC-3: Compact binary coalescences observed by LIGO and Virgo during the second part of the third observing run, Phys. Rev. X **13**, 041039 (2023).

[7] B. P. Abbott *et al.* (LIGO Scientific and Virgo Collaborations), Tests of general relativity with GW150914, Phys. Rev. Lett. **116**, 221101 (2016); **121**, 129902(E) (2018).

[8] B. P. Abbott *et al.* (LIGO Scientific and Virgo Collaborations), Tests of general relativity with GW170817, Phys. Rev. Lett. **123**, 011102 (2019).

[9] B. P. Abbott *et al.* (LIGO Scientific and Virgo Collaborations), Tests of general relativity with the binary black hole signals from the LIGO-Virgo catalog GWTC-1, Phys. Rev. D **100**, 104036 (2019).

[10] R. Abbott *et al.* (LIGO Scientific and Virgo Collaborations), Tests of general relativity with binary black holes from the second LIGO-Virgo gravitational-wave transient catalog, Phys. Rev. D **103**, 122002 (2021).

[11] R. Abbott *et al.* (LIGO Scientific, Virgo, and KAGRA Collaborations), Tests of general relativity with GWTC-3, arXiv:2112.06861.

[12] C. M. Will, The confrontation between general relativity and experiment, Living Rev. Relativity **17**, 4 (2014).

[13] I. H. Stairs, Testing general relativity with pulsar timing, Living Rev. Relativity **6**, 5 (2003).

[14] N. Wex, Testing relativistic gravity with radio pulsars, arXiv:1402.5594.

[15] M. Kramer *et al.*, Strong-field gravity tests with the double pulsar, Phys. Rev. X **11**, 041050 (2021).

[16] R. Abuter *et al.* (GRAVITY Collaboration), Detection of the gravitational redshift in the orbit of the star S2 near the galactic centre massive black hole, Astron. Astrophys. **615**, L15 (2018).

[17] T. Do *et al.*, Relativistic redshift of the star S0-2 orbiting the galactic center supermassive black hole, Science **365**, 664 (2019).

[18] K. Akiyama *et al.* (Event Horizon Telescope Collaboration), First M87 Event Horizon Telescope Results. IV. Imaging the central supermassive black hole, Astrophys. J. Lett. **875**, L4 (2019).

[19] M. Okounkova, L. C. Stein, M. A. Scheel, and D. A. Hemberger, Numerical binary black hole mergers in dynamical Chern-Simons gravity: Scalar field, Phys. Rev. D **96**, 044020 (2017).

[20] M. Okounkova, L. C. Stein, J. Moxon, M. A. Scheel, and S. A. Teukolsky, Numerical relativity simulation of GW150914 beyond general relativity, Phys. Rev. D **101**, 104016 (2020).

[21] M. Okounkova, Numerical relativity simulation of GW150914 in Einstein dilaton Gauss-Bonnet gravity, Phys. Rev. D **102**, 084046 (2020).

[22] R. N. Lang, Compact binary systems in scalar-tensor gravity. III. Scalar waves and energy flux, Phys. Rev. D **91**, 084027 (2015).

[23] N. Sennett, S. Marsat, and A. Buonanno, Gravitational waveforms in scalar-tensor gravity at 2PN relative order, Phys. Rev. D **94**, 084003 (2016).

[24] L. Bernard, Dynamics of compact binary systems in scalar-tensor theories: II. Center-of-mass and conserved quantities to 3PN order, Phys. Rev. D **99**, 044047 (2019).

[25] N. Sennett, R. Brito, A. Buonanno, V. Gorbenko, and L. Senatore, Gravitational-wave constraints on an effective field-theory extension of general relativity, Phys. Rev. D **102**, 044056 (2020).

[26] F.-L. Julié and E. Berti, Post-Newtonian dynamics and black hole thermodynamics in Einstein-scalar-Gauss-Bonnet gravity, Phys. Rev. D **100**, 104061 (2019).

[27] N. J. Cornish and T. B. Littenberg, BayesWave: Bayesian inference for gravitational wave bursts and instrument glitches, Classical Quantum Gravity **32**, 135012 (2015).

[28] S. Ghonge, K. Chatziioannou, J. A. Clark, T. Littenberg, M. Millhouse, L. Cadonati, and N. Cornish, Reconstructing gravitational wave signals from binary black hole mergers with minimal assumptions, Phys. Rev. D **102**, 064056 (2020).

[29] S. Roy, Nonorthogonal wavelet transformation for reconstructing gravitational wave signals, Phys. Rev. Res. **4**, 033078 (2022).

[30] A. Ghosh *et al.*, Testing general relativity using golden black-hole binaries, Phys. Rev. D **94**, 021101 (2016).

[31] A. Maselli, P. Pani, L. Gualtieri, and E. Berti, Parametrized ringdown spin expansion coefficients: A data-analysis framework for black-hole spectroscopy with multiple events, Phys. Rev. D **101**, 024043 (2020).

[32] M. Agathos, W. Del Pozzo, T. G. F. Li, C. Van Den Broeck, J. Veitch, and S. Vitale, TIGER: A data analysis pipeline for testing the strong-field dynamics of general relativity with gravitational wave signals from coalescing compact binaries, Phys. Rev. D **89**, 082001 (2014).

[33] J. Meidam, M. Agathos, C. Van Den Broeck, J. Veitch, and B. S. Sathyaprakash, Testing the no-hair theorem with black hole ringdowns using TIGER, Phys. Rev. D **90**, 064009 (2014).

[34] A. K. Mehta, A. Buonanno, R. Cotesta, A. Ghosh, N. Sennett, and J. Steinhoff, Tests of general relativity with gravitational-wave observations using a flexible theory-independent method, Phys. Rev. D **107**, 044020 (2023).

[35] M. Saleem, S. Datta, K. G. Arun, and B. S. Sathyaprakash, Parametrized tests of post-Newtonian theory using principal component analysis, Phys. Rev. D **105**, 084062 (2022).

[36] S. Klimenko, I. Yakushin, A. Mercer, and G. Mitselmakher, Coherent method for detection of gravitational wave bursts, Classical Quantum Gravity **25**, 114029 (2008).

[37] M. Drago, S. Klimenko, C. Lazzaro, E. Milotti, G. Mitselmakher, V. Necula, B. O'Brian, G. A. Prodi, F. Salemi, M. Szczepanczyk, S. Tiwari, V. Tiwari, V. Gayathri, G. Vedovato, and I. Yakushin, Coherent Wave-Burst, a pipeline for unmodeled gravitational-wave data analysis, SoftwareX **14**, 100678 (2021).

[38] R. Lynch, S. Vitale, R. Essick, E. Katsavounidis, and F. Robinet, Information-theoretic approach to the gravitational-wave burst detection problem, Phys. Rev. D **95**, 104046 (2017).

[39] F. Robinet, N. Arnaud, N. Leroy, A. Lundgren, D. Macleod, and J. McIver, Omicron: A tool to characterize transient noise in gravitational-wave detectors, SoftwareX **12**, 100620 (2020).

[40] C. Messick *et al.*, Analysis framework for the prompt discovery of compact binary mergers in gravitational-wave data, Phys. Rev. D **95**, 042001 (2017).

[41] L. Tsukada *et al.*, Improved ranking statistics of the GstLAL inspiral search for compact binary coalescences, Phys. Rev. D **108**, 043004 (2023).

[42] F. Aubin *et al.*, The MBTA pipeline for detecting compact binary coalescences in the third LIGO–Virgo observing run, Classical Quantum Gravity **38**, 095004 (2021).

[43] S. A. Usman *et al.*, The PyCBC search for gravitational waves from compact binary coalescence, Classical Quantum Gravity **33**, 215004 (2016).

[44] A. H. Nitz, T. Dal Canton, D. Davis, and S. Reyes, Rapid detection of gravitational waves from compact binary mergers with PyCBC live, Phys. Rev. D **98**, 024050 (2018).

[45] T. Dal Canton, A. H. Nitz, B. Gadre, G. S. Cabourn Davies, V. Villa-Ortega, T. Dent, I. Harry, and L. Xiao, Real-time search for compact binary mergers in Advanced LIGO and Virgo's third observing run using PyCBClive, Astrophys. J. **923**, 254 (2021).

[46] Q. Chu *et al.*, SPIIR online coherent pipeline to search for gravitational waves from compact binary coalescences, Phys. Rev. D **105**, 024023 (2022).

[47] H. Narola, S. Roy, and A. S. Sengupta, Beyond general relativity: Designing a template-based search for exotic gravitational wave signals, Phys. Rev. D **107**, 024017 (2023).

[48] T. A. Apostolatos, Search templates for gravitational waves from precessing, inspiraling binaries, Phys. Rev. D **52**, 605 (1995).

[49] B. J. Owen, Search templates for gravitational waves from inspiraling binaries: Choice of template spacing, Phys. Rev. D **53**, 6749 (1996).

[50] N. Yunes, P. Pani, and V. Cardoso, Gravitational waves from quasicircular extreme mass-ratio inspirals as probes of scalar-tensor theories, Phys. Rev. D **85**, 102003 (2012).

[51] B. P. Abbott *et al.* (LIGO Scientific and Virgo Collaborations), Tests of general relativity with GW170817, Phys. Rev. Lett. **123**, 011102 (2019).

[52] B. J. Owen and B. S. Sathyaprakash, Matched filtering of gravitational waves from inspiraling compact binaries: Computational cost and template placement, Phys. Rev. D **60**, 022002 (1999).

[53] R. Prix, Template-based searches for gravitational waves: Efficient lattice covering of flat parameter spaces, Classical Quantum Gravity **24**, S481 (2007).

[54] T. Cokelaer, A template bank to search for gravitational waves from inspiralling compact binaries. II. Phenomenological model, Classical Quantum Gravity **24**, 6227 (2007).

[55] D. A. Brown, I. Harry, A. Lundgren, and A. H. Nitz, Detecting binary neutron star systems with spin in advanced gravitational-wave detectors, Phys. Rev. D **86**, 084017 (2012).

[56] J. Roulet, L. Dai, T. Venumadhav, B. Zackay, and M. Zaldarriaga, Template bank for compact binary coalescence searches in gravitational wave data: A general geometric placement algorithm, Phys. Rev. D **99**, 123022 (2019).

[57] C. Hanna *et al.*, Binary tree approach to template placement for searches for gravitational waves from compact binary mergers, Phys. Rev. D **108**, 042003 (2023).

[58] B. Allen, Optimal template banks, Phys. Rev. D **104**, 042005 (2021).

[59] I. W. Harry, B. Allen, and B. S. Sathyaprakash, A stochastic template placement algorithm for gravitational wave data analysis, Phys. Rev. D **80**, 104014 (2009).

[60] S. Babak, Building a stochastic template bank for detecting massive black hole binaries, Classical Quantum Gravity **25**, 195011 (2008).

[61] B. Allen, Performance of random template banks, Phys. Rev. D **105**, 102003 (2022).

[62] S. Roy, A. S. Sengupta, and N. Thakor, Hybrid geometric-random template-placement algorithm for gravitational wave searches from compact binary coalescences, Phys. Rev. D **95**, 104045 (2017).

[63] S. Roy, A. S. Sengupta, and P. Ajith, Effectual template banks for upcoming compact binary searches in Advanced-LIGO and Virgo data, Phys. Rev. D **99**, 024048 (2019).

[64] S. Roy, A. Sankar Sengupta, and P. Ajith, Geometric-stochastic template banks for gravitational wave searches from compact binaries in Advanced-LIGO data, in *Proceedings of the 42nd COSPAR Scientific Assembly, Pasadena, California, USA* (2018), Vol. 42, pp. E1.15–36–18.

[65] C. Capano, I. Harry, S. Privitera, and A. Buonanno, Implementing a search for gravitational waves from binary black holes with nonprecessing spin, Phys. Rev. D **93**, 124007 (2016).

[66] T. Dal Canton and I. W. Harry, Designing a template bank to observe compact binary coalescences in Advanced LIGO's second observing run, arXiv:1705.01845.

[67] N. Indik, H. Fehrmann, F. Harke, B. Krishnan, and A. B. Nielsen, Reducing the number of templates for aligned-spin compact binary coalescence gravitational wave searches using metric-agnostic template nudging, Phys. Rev. D **97**, 124008 (2018).

[68] D. R. Lorimer and M. Kramer, *Handbook of Pulsar Astronomy* (Cambridge University Press, 2004), Vol. 4, ISBN 10 0521828236.

[69] L. Blanchet, Gravitational radiation from post-Newtonian sources and inspiralling compact binaries, Living Rev. Relativity **17**, 2 (2014).

[70] E. Poisson and C. M. Will, Gravitational waves from inspiraling compact binaries: Parameter estimation using second postNewtonian wave forms, Phys. Rev. D **52**, 848 (1995).

[71] A. Buonanno, B. Iyer, E. Ochsner, Y. Pan, and B. S. Sathyaprakash, Comparison of post-Newtonian templates for compact binary inspiral signals in gravitational-wave detectors, Phys. Rev. D **80**, 084043 (2009).

[72] C. K. Mishra, K. G. Arun, B. R. Iyer, and B. S. Sathyaprakash, Parametrized tests of post-Newtonian theory using Advanced LIGO and Einstein Telescope, Phys. Rev. D **82**, 064010 (2010).

[73] T. G. F. Li, W. Del Pozzo, S. Vitale, C. Van Den Broeck, M. Agathos, J. Veitch, K. Grover, T. Sidery, R. Sturani, and A. Vecchio, Towards a generic test of the strong field dynamics of general relativity using compact binary coalescence, Phys. Rev. D **85**, 082003 (2012).

[74] J. Meidam *et al.*, Parametrized tests of the strong-field dynamics of general relativity using gravitational wave signals from coalescing binary black holes: Fast likelihood calculations and sensitivity of the method, Phys. Rev. D **97**, 044033 (2018).

[75] B. S. Sathyaprakash and S. V. Dhurandhar, Choice of filters for the detection of gravitational waves from coalescing binaries, Phys. Rev. D **44**, 3819 (1991).

[76] S. V. Dhurandhar and B. S. Sathyaprakash, Choice of filters for the detection of gravitational waves from coalescing binaries. 2. Detection in colored noise, Phys. Rev. D **49**, 1707 (1994).

[77] B. Allen, W. G. Anderson, P. R. Brady, D. A. Brown, and J. D. E. Creighton, FINDCHIRP: An algorithm for detection of gravitational waves from inspiraling compact binaries, Phys. Rev. D **85**, 122006 (2012).

[78] I. W. Harry, A. H. Nitz, D. A. Brown, A. P. Lundgren, E. Ochsner, and D. Keppel, Investigating the effect of precession on searches for neutron-star–black-hole binaries with Advanced LIGO, Phys. Rev. D **89**, 024010 (2014).

[79] E. K. Porter, Computational resources to filter gravitational wave data with p-approximant templates, Classical Quantum Gravity **19**, 4343 (2002).

[80] P. Virtanen *et al.*, SciPy 1.0–Fundamental algorithms for scientific computing in Python, Nat. Methods **17**, 261 (2020).

[81] I. Harry and A. Lundgren, Failure of the Fisher matrix when including tidal terms: Considering construction of template banks of tidally deformed binary neutron stars, Phys. Rev. D **104**, 043008 (2021).

[82] H. Wang, I. Harry, A. Nitz, and Y.-M. Hu, The challenge of eccentricity when observing stellar-mass binary black holes with space-based gravitational wave detectors, Phys. Rev. D **109**, 063029 (2024).

[83] A. A. Shoom, P. K. Gupta, B. Krishnan, A. B. Nielsen, and C. D. Capano, Testing the post-Newtonian expansion with GW170817, Gen. Relativ. Gravit. **55**, 55 (2023).

[84] M. Vallisneri, J. Kanner, R. Williams, A. Weinstein, and B. Stephens, The LIGO open science center, J. Phys. Conf. Ser. **610**, 012021 (2015).

[85] LIGO Scientific Collaboration, LIGO Algorithm Library—LALSuite, free software (GPL) (2023), 10.7935/GT1W-FZ16.

[86] A. Nitz *et al.*, GWASTRO/PYCBC: v2.2.0 release of PYCBC (2023).

[87] C. R. Harris *et al.*, Array programming with NumPy, Nature (London) **585**, 357 (2020).

[88] J. D. Hunter, Matplotlib: A 2D graphics environment, Comput. Sci. Eng. **9**, 90 (2007).

[89] K. G. Arun, A. Buonanno, G. Faye, and E. Ochsner, Higher-order spin effects in the amplitude and phase of gravitational waveforms emitted by inspiraling compact binaries: Ready-to-use gravitational waveforms, Phys. Rev. D **79**, 104023 (2009); **84**, 049901(E) (2011).

[90] A. Bohé, S. Marsat, and L. Blanchet, Next-to-next-to-leading order spin-orbit effects in the gravitational wave flux and orbital phasing of compact binaries, Classical Quantum Gravity **30**, 135009 (2013).

[91] A. Bohé, G. Faye, S. Marsat, and E. K. Porter, Quadratic-in-spin effects in the orbital dynamics and gravitational-wave energy flux of compact binaries at the 3PN order, Classical Quantum Gravity **32**, 195010 (2015).